

# The longitudinal conductance of mesoscopic Hall samples with arbitrary disorder and periodic modulations

Chenggang Zhou

*Department of Electrical Engineering, Princeton University, Princeton NJ 08544, USA*

Mona Berciu

*Department of Physics and Astronomy, University of British Columbia, Vancouver, BC V6T 1Z1, Canada*

(Dated: February 2, 2008)

We use the Kubo-Landauer formalism to compute the longitudinal (two-terminal) conductance of a two dimensional electron system placed in a strong perpendicular magnetic field, and subjected to periodic modulations and/or disorder potentials. The scattering problem is recast as a set of inhomogeneous, coupled linear equations, allowing us to find the transmission probabilities from a finite-size system computation; the results are exact for non-interacting electrons. Our method fully accounts for the effects of the disorder and the periodic modulation, irrespective of their relative strength, as long as Landau level mixing is negligible. In particular, we focus on the interplay between the effects of the periodic modulation and those of the disorder. This appears to be the relevant regime to understand recent experiments [S. Melinte *et al*, Phys. Rev. Lett. **92**, 036802 (2004)], and our numerical results are in qualitative agreement with these experimental results. The numerical techniques we develop can be generalized straightforwardly to many-terminal geometries, as well as other multi-channel scattering problems.

PACS numbers: 73.43.Cd

## I. INTRODUCTION

A significant amount of research has been devoted to the study of the effect of a periodic potential on a two dimensional electron system (2DES) placed in large perpendicular magnetic fields. On the theory side, the so-called Hofstadter butterfly<sup>1</sup> – the fractal energy spectrum associated with the periodically modulated 2DES, in the absence of disorder – had been predicted and studied even before Hofstadter's seminal paper.<sup>2,3,4,5</sup> Later, the transport properties of such systems were studied by Štředa, MacDonald and others.<sup>6,7,8,9</sup> After the discovery of the Integer Quantum Hall Effect (IQHE),<sup>10</sup> experimental results started to become available.<sup>11,12</sup> Pfannkuche and Gerhardt put forward a detailed theoretical treatment of transport properties, including disorder effects.<sup>13</sup> Their theory is analogous to the self-consistent Born approximation (SCBA),<sup>14</sup> and it suggests that the splitting of one single Landau band into several subbands by the periodic modulation can in principle be observed from measurements of the longitudinal conductance  $\sigma_{xx}$ . The effect of disorder on the fractal structure was found to be similar to its effect on the Landau level (LL) structure (responsible for the appearance of IQHE): subbands in each Landau level are broadened by disorder, but energy gaps or pseudo gaps are still open if the disorder is small compared to the amplitude of the periodic potential. As the Fermi energy sweeps through a subband, the longitudinal conductance has a maximum and the Hall conductance shows a staircase-like jump if the Chern numbers in the neighboring gaps are different. Thus, the Hall conductance is expected to follow a nontrivial sequence of integer multiples of  $e^2/h$ ,<sup>15</sup> whereas the longitudinal conductance has a series of peaks and valleys as the Fermi

level moves through different subbands and gaps.

A recent experiment<sup>16</sup> on a high-quality, periodically modulated 2DES shows interesting new features in the longitudinal conductance, although the periodic potential is too weak to produce well-separated subbands (or, equivalently, disorder is strong enough to fill in all subgaps in the fractal structure of each Landau level). Even in this case, the longitudinal conductance exhibits reproducible oscillatory features in the presence of the weak periodic modulation, instead of the single smooth Lorentz peak of the unpatterned samples. To our knowledge, this regime of strong disorder and weak periodic modulation has not been investigated in the literature, and therefore these recent experimental results do require theoretical interpretation. In recent work,<sup>17</sup> we analyzed the spectrum and nature (localized or extended) of electronic states in such a regime, and showed that simple arguments based on these results provide a qualitative explanation of the experimental observations.

In this study, we present a numerical calculation of the longitudinal conductance based on models appropriate for the type of samples used in the experiment of Ref. [16]. Our model includes a disorder potential and a periodic potential with either square or triangular symmetry, with arbitrary relative strengths. In this work we assume that these potentials are small enough that Landau level mixing is negligible, although the methods we develop can be trivially generalized to take such mixing into account. Unlike previous theoretical studies dealing with disorder effects in QHE, which performed average over disorder at the onset of the calculation so that all computed response functions are disorder-averaged, we calculate the longitudinal conductance from first principles for a given disorder realization. This is necessary

because the features observed in this experiment<sup>16</sup> are believed to be sample-specific. Our calculation is based on the Kubo-Landauer formalism.<sup>28</sup> Our method is in principle valid for finite systems with any type of disorder and/or periodic potentials, although computational times vary with the sample size and degree of sparseness of the Hamiltonian. Regrettably, we have no detailed microscopic knowledge of the disorder present in these samples and the details regarding their connections to the external leads; this prevents us from performing meaningful quantitative comparisons with the experiment. However, the results we obtain for different realizations of disorder allow us to qualitatively explain the physics responsible for the new features in the longitudinal conductance, and to reinforce the arguments offered in our previous work.<sup>17</sup>

The paper is organized as follows: in Section II we present the method used for the calculation and the relevant theoretical considerations. The numerical results are presented in Section III, while Section IV contains our conclusions and discussions.

## II. THE NUMERICAL METHOD: KUBO-LANDAUER FORMALISM

### A. The model

We consider a two-dimensional Hall sample of rectangular shape, of size  $L_x \times L_y$ , with cyclic boundary conditions in the  $y$ -direction and open boundary condition in the  $x$ -direction, characteristic of a two-terminal geometry. Typical sizes we consider are on the order of  $3\mu\text{m} \times 3\mu\text{m}$ . A large magnetic field  $\mathbf{B}$  of up to 10T is applied in the  $z$ -direction, perpendicular to the 2DES. A rough estimate shows that the degeneracy  $N$  of each Landau level (LL) is of order  $10^4$ , defining the size of the matrix to be diagonalized to be  $10^4 \times 10^4$ . For such large-size matrices direct diagonalization is time-consuming, therefore we look for alternative approaches with a better scaling behavior for large systems. On the other hand, the sample size is still small compared to that of the experimental sample, which is about  $20\mu\text{m} \times 20\mu\text{m}$ . As a result, care must be taken in interpreting the numerical results. In principle it is possible to increase the values of  $L_x$  and  $L_y$ , however serious numerical difficulties arise when the system size is much larger than the ones we consider (these issues are discussed in section II C).

The Hamiltonian of the non-interacting electrons confined in the 2DES is

$$\mathcal{H}_s = \frac{1}{2m} \left( \mathbf{p} + \frac{e}{c} \mathbf{A} \right)^2 - \frac{1}{2} g \mu_B \vec{\sigma} \cdot \mathbf{B} + V_d(x, y) + V_p(x, y).$$

where  $V_d$  and  $V_p$  are the disorder and the periodic potentials, respectively. We use the Landau gauge  $\mathbf{A} = (0, Bx, 0)$  throughout this paper, and the complete set of eigenfunctions for the  $n^{\text{th}}$  Landau level:

$$\langle \mathbf{r} | n, X, \sigma \rangle = \frac{e^{-i \frac{Xy}{l^2}}}{\sqrt{L_y}} e^{-\frac{1}{2l^2}(x-X)^2} \frac{H_n\left(\frac{x-X}{l}\right)}{\sqrt{2^n n! \sqrt{\pi} l}} \chi_\sigma \quad (1)$$

where  $l = \sqrt{\frac{\hbar c}{eB}}$  is the magnetic length and  $H_n(x)$  are Hermite polynomials. In the rest of the paper, we concentrate on one of the spin-polarized lowest Landau levels (LLL), therefore we set  $n = 0$ . This is justified because in the experiment both the disorder and the periodic potentials are estimated to be much smaller than the cyclotron energy  $\hbar\omega$  and the Zeeman splitting,<sup>18</sup> so that Landau level mixing can be safely ignored.<sup>16,17</sup> Imposing cyclic boundary condition in the  $y$ -direction leads to the restriction  $X_j = j2\pi l^2/L_y$ ,  $j = 1, \dots, N$ .  $X_j$ , the guiding center, characterizes the location at which individual basis states are centered along  $x$ -axis [see Eq. (1)]. Since  $X_j$  can vary between 0 and  $L_x$ , the degeneracy of each spin-polarized LLL is  $N = L_x L_y / (2\pi l^2)$ .

Let us define  $c_j^\dagger$  to be the creation operator for an electron in the LLL:  $c_j^\dagger |0\rangle = |X_j\rangle$  (the indexes  $n = 0$  and  $\sigma$  will be suppressed from now on). In the absence of Landau level mixing, the Hamiltonian  $\mathcal{H}_s$  projected on the subspace of the spin-polarized LLL becomes:

$$\mathcal{H}_s = \frac{\hbar\omega_c - g\mu_B B\sigma}{2} \sum_{j=1}^N c_j^\dagger c_j + \sum_{i=1}^N \sum_{j=1}^N \langle X_i | V_d + V_p | X_j \rangle \cdot c_i^\dagger c_j \quad (2)$$

This looks like a one-dimensional(1D) hopping Hamiltonian, and this is a very appropriate comparison if one keeps in mind that the state  $|X_i\rangle$  is indeed localized within a distance  $l$  of  $X_i = i2\pi l^2/L_y$ .

In order to calculate the matrix elements for the disorder and the periodic potentials, we use the identity

$$\langle X_i | e^{i\mathbf{q} \cdot \mathbf{r}} | X_j \rangle = \delta_{X_i, X_j - q_y l^2} e^{\frac{i}{2} q_x (X_i + X_j)} e^{-\frac{i}{2} Q} \quad (3)$$

where  $Q = \frac{1}{2} l^2 (q_x^2 + q_y^2)$ . (The generalization for higher Landau levels and/or Landau level mixing is straightforward, see for instance Ref. [13]). Let us now consider each type of potential separately.

The periodic potential can be expanded as:

$$V_p(\mathbf{r}) = \sum_{\mathbf{g}} V_{\mathbf{g}} e^{i\mathbf{r} \cdot \mathbf{g}}. \quad (4)$$

where  $V_{\mathbf{g}} = V_{-\mathbf{g}}^*$  because  $V(\mathbf{r})$  is real, and  $\{\mathbf{g}\}$  are the reciprocal vectors associated with the Bravais lattice. For a square potential, we use  $V_{\mathbf{g}} = A$  for all four shortest reciprocal vectors  $\mathbf{g} = (\pm 2\pi/a, 0), (0, \pm 2\pi/a)$ , where  $a$  is lattice constant, and zero otherwise. Higher order components can also be included in the same formalism, but result in longer computational time and no qualitative changes. Similarly, for a triangular potential we define  $V_{\mathbf{g}} = -A$  for all six shortest reciprocal vectors  $\mathbf{g} = 4\pi/\sqrt{3}a(\pm 1, 0), 2\pi/\sqrt{3}a(\pm 1, \pm \sqrt{3})$ , and zero otherwise. The minus sign appears here in order to have the minima on the sites of the triangular lattice, as explained in Ref. [17]. In both cases the projection of  $\mathbf{g}$  on the  $y$ -axis is either 0 or  $\pm \frac{2\pi}{a}$ . This particular orientation allows us to treat these two potentials similarly, since it follows that both types of periodic potentials only couple a state

$|X_j\rangle$  to itself and to  $|X_j \pm 2\pi l^2/a\rangle$  [see Eq. (3)]. Since  $|X_j \pm 2\pi l^2/a\rangle$  must be in the basis considered,  $2\pi l^2/a$  must be an integer multiple of  $2\pi l^2/L_y$ , i.e.  $L_y$  is an integer multiple of  $a$ . This is consistent with the periodic boundary conditions along the  $y$ -axis.

We introduce the integer  $N_c = L_y/a$ . From the previous discussion, it follows that the periodic potential couples a state  $X_j$  only to itself, and to the states  $X_{j \pm N_c}$ . As a result, we can divide the total  $N$  states of the LLL into  $N_c$  subclasses (henceforth called the conduction channels) using the unique decomposition  $j = iN_c + n$ , where  $i > 0$  is an integer, and  $1 \leq n \leq N_c$ . The periodic potential couples only states in the same channel  $n$ ; these states are distributed equidistantly across the sample, between the  $x = 0$  and the  $x = L_x$  edges, and can carry currents across the sample (hence the name “conduction channels”). For simplicity, we require that each channel has the same overall number of states, i.e. the total degeneracy  $N$  is an integer multiple of the number of channels  $N_c$ ,  $N = pN_c$ . (This condition can be easily relaxed.) This imposes a constraint  $L_x = p(2\pi l^2)/a$  on the values allowed for  $L_x$ . For the typical sample sizes we consider, the constraints on  $L_x$  and  $L_y$  require only minimal adjustments. For instance, we use  $a = 39$  nm,<sup>16</sup> and therefore a sample with  $L_x \approx L_y \approx 3$   $\mu$ m will have around  $N_c = 70$  channels, with around  $p = 150$  states per channel. For different values of the magnetic field (different  $l$  values) the length  $L_x$  can be kept fixed within a few nm by slightly adjusting the value of  $p$ .

For later convenience, we re-label the creation operators for states in the LLL as  $c_j^\dagger \rightarrow c_{i,n}^\dagger$ , where  $j = iN_c + n$ ,  $1 \leq n \leq N_c$ . It follows that the periodic potential projected on the spin-polarized LLL takes the simple form

$$\hat{V}_p = \sum_{n=1}^{N_c} \left[ \sum_{i=1}^p \epsilon_{i,n} c_{i,n}^\dagger c_{i,n} + \sum_{i=1}^{p-1} \left( t_{i,n} c_{i,n}^\dagger c_{i+1,n} + h.c. \right) \right], \quad (5)$$

where for the square potential, we have:

$$\epsilon_{i,n} = 2Ae^{-(\frac{\pi l}{a})^2} \cos \left[ \left( i + \frac{n}{N_c} \right) \left( \frac{2\pi l}{a} \right)^2 \right], \quad (6a)$$

$$t_{i,n} = 2Ae^{-(\frac{\pi l}{a})^2}, \quad (6b)$$

and for the triangular potential, we have:

$$\epsilon_{i,n} = -2Ae^{-\frac{4}{3}(\frac{\pi l}{a})^2} \cos \left[ \frac{8\pi^2 l^2}{\sqrt{3}a^2} \left( i + \frac{n}{N_c} \right) \right], \quad (7a)$$

$$t_{i,n} = -2Ae^{-\frac{4}{3}(\frac{\pi l}{a})^2} \cos \left[ \frac{4\pi^2 l^2}{\sqrt{3}a^2} \left( i + \frac{n}{N_c} + \frac{1}{2} \right) \right]. \quad (7b)$$

From Equations (6) and (7), it is apparent that the parameter controlling the band-structure (in the absence of disorder) is the ratio  $\phi/\phi_0 = \mathcal{A}/(2\pi l^2)$ , where  $\phi_0 = hc/e$  is the elementary flux, and  $\phi = B\mathcal{A}$  is the magnetic flux through the unit cell of the periodic potential.  $\mathcal{A} = a^2$  or  $a^2\sqrt{3}/2$  for square or triangular potentials respectively.

In particular, if  $\phi/\phi_0 = q/p$ , where  $q$  and  $p$  are mutually prime integers, the original LL splits into  $q$  sub-bands.<sup>1,19</sup>

In the absence of disorder, there is no mixing between different channels [see Eq. (5)], and the longitudinal current is just a sum of the currents carried across the sample through the individual conduction channels. However, disorder introduces scattering between different channels. First principles modeling of the disorder in real samples is a very difficult and numerically intensive problem.<sup>20,21,22</sup> As a result, we generate the disorder potential using two simple phenomenological models described in detail in Ref. [17]. One is a simple addition of random gaussians, while the second model attempts to estimate the proper energy scale from considerations of the Coulomb attraction between electrons and their donors. Both models generate smooth disorder potentials, i.e. with a length scale of more than 100 nm, which is very large compared with the typical magnetic length  $l$  ( $l \sim 8$  nm when  $B \sim 10$  T). Such long-wavelength disorder is believed to be dominant in high-quality samples, as the one studied in Ref. [16]. The standard deviation is estimated to be 2 to 3 meV, much smaller than the typical cyclotron energy.<sup>17</sup> We Fourier-decompose the disorder potential, and use Eq.(3) to compute its matrix elements. The periodic boundary condition in the  $y$ -direction implies that the allowed Fourier components are  $q_y = 2\pi m/L_y$ , which introduces matrix elements between any pair of states  $|X_i\rangle$  and  $|X_{i \pm m}\rangle$ , where  $m$  is an arbitrary integer. It follows that different conduction channels are now coupled by disorder. The small  $\mathbf{q}$  Fourier components of the disorder potential are very important, since they describe the long wavelength features of the disorder potential. High values of  $\mathbf{q}$ , on the other hand, describe short wavelength features of the disorder, which are not well captured by our simple phenomenological models. As a result, we use a cutoff value of  $|m| < 36$  for Fourier components of the disorder potential kept. This value is large enough to allow basically exact reconstruction of the disorder potential (see relevant discussion in Ref. [17]) but also small enough so that the Hamiltonian matrix is still very sparse. With this cutoff and in the absence of LL mixing, the disorder potential has the general form:

$$V_d = \sum_{n,n'=1}^{N_c} \sum_{i,i'=1}^p v_{i,n;i',n'} c_{i,n}^\dagger c_{i',n'}, \quad (8)$$

where  $v_{i,n;i',n'}$  is non-vanishing only for states within a distance  $|(i-i')N_c + (n-n')| \leq 36$  of each other.

From Equations (2), (5) and (8) it follows that the total Hamiltonian for the sample is:

$$\begin{aligned} \mathcal{H}_s = & \sum_{n=1}^{N_c} \left[ \sum_{i=1}^p \epsilon_{i,n} c_{i,n}^\dagger c_{i,n} + \sum_{i=1}^{p-1} \left( t_{i,n} c_{i,n}^\dagger c_{i+1,n} + h.c. \right) \right] \\ & + \sum_{n,n'=1}^{N_c} \sum_{i,i'=1}^p v_{i,n;i',n'} c_{i,n}^\dagger c_{i',n'}, \end{aligned} \quad (9)$$

where the overall energy shift  $(\hbar\omega_c - g\mu_B B\sigma)/2$  associated with the LLL is absorbed in a redefined chemical potential. This Hamiltonian can be efficiently generated and stored as a column compressed sparse matrix. In principle, we can directly compute the eigenvalues and eigenfunctions of this Hamiltonian, and calculate the corresponding Thouless number, characterizing its longitudinal conductance.<sup>23</sup> However, this is numerically very time-consuming. Instead, we use the Kubo-Landauer<sup>24,25,26,27,28,29</sup> formula for the longitudinal conductance (details in section II B) which requires the computation of various transmission coefficients through the sample. The main idea is to link the longitudinal conductance to the total probability that an electron injected into the sample at  $x = 0$  arrives at  $x = L_x$ , or vice versa.

In order to compute these transmission coefficients, it is necessary to connect the sample to external metallic leads which allow us to inject into and extract electrons from the sample. We model each external lead as a collection of independent, semi-infinite 1D tight-binding chains, as illustrated in Figure 1. In reality, the leads have, of course, higher dimensionality than one. One way to simulate this would be to add bonds (hopping) between the various 1D chains. We do not add these extra bonds for the following reason: the eigenstates of any lead with complex geometry in the transverse direction have the general structure  $E_{k,n} = \epsilon_n(k) + u_n$ . Here,  $k$  is a quasimomentum associated with the longitudinal direction, a good quantum number given the translational invariance along this direction, and  $n$  is some discrete set of quantum numbers characterizing the discrete transverse modes supported by the particular geometry of the lead cross-section. In other words, any perfectly metallic higher-dimensional lead reduces to a collection of independent 1D leads (or channels), whose dispersions can be simulated by an appropriate choice of 1D tight-binding chains.<sup>30</sup> The question, then, is how many channels are in each lead, and how are they connected to the states in the sample. Since we have no detailed knowledge regarding the leads, and since one hopes that the main features of the longitudinal conductance will come from the sample itself, not the details of the lead modeling, we choose the following very simple solution: we assume that both the left and right-side leads have precisely  $N_c$  channels, and each one of these channels couples identically to one of the conduction channels inside the sample. This is the simplest model that satisfies several criteria: (i) the leads are perfect conductors; (ii) the conductance of the leads is not less than the maximum conductance of the sample;<sup>31</sup> (iii) each conduction channel in the sample has equal coupling to the leads; (iv) transmission and reflection coefficients can be easily defined and computed. However, any other more complex model for the connection of the sample to the external leads can be investigated with the formalism we develop here.

Let us index with  $n = 1, 2, \dots, N_c$  the  $N_c$  independent 1D channels of each semi-infinite lead, and let  $c_{i,n}^\dagger$  be the creation operator for an electron at site  $i$  of the  $n^{\text{th}}$  1D

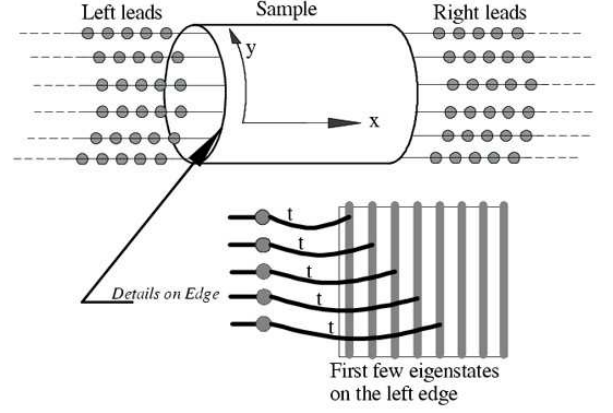


FIG. 1: A sketch of the model geometry of the Hall sample with periodic boundary conditions in the  $y$ -direction, and its contact to leads on both  $x$ -axis ends. The lower diagram shows a detailed view of the left edge. The first  $N_c$  eigenstates  $|X_1\rangle, |X_2\rangle, \dots, |X_{N_c}\rangle$  near the edge belong to different conduction channels. We assume that each such conduction channel is attached to external leads at both edges of the sample.

chain. We distinguish between the left and right leads by requiring that  $i \leq 0$  for the left channels, respectively  $i > p$  for the right channels. This notation also avoids any confusion between these operators, and the operators creating electrons in LLL states inside the sample, which correspond to  $1 \leq i \leq p$ . The spin-index is suppressed everywhere, since in the absence of magnetic impurities electrons with different spins travel independently.

The Hamiltonian describing the external leads and their coupling to the sample is then:

$$\mathcal{H}_L = \sum_{n=1}^{N_c} \left( \sum_{i=-\infty}^{-1} + \sum_{i=p+1}^{\infty} \right) \left[ -t(c_{i,n}^\dagger c_{i+1,n} + c_{i+1,n} c_{i,n}^\dagger) \right. \\ \left. + \epsilon_0 c_{i,n}^\dagger c_{i,n} \right] - t \sum_{n=1}^{N_c} \left( c_{0,n}^\dagger c_{1,n} + c_{p,n}^\dagger c_{p+1,n} + h.c. \right)$$

Here,  $t$  and  $\epsilon_0$  are adjustable parameters, whose selection is discussed in section II C. Our model of the leads is thus similar to those employed for the study of molecular conductance,<sup>32,33,34</sup> where tight-binding chains are used to simulate the gold contacts. In fact, we treat our Hall sample as a big molecule wired to contacts. As we demonstrate in the following, we only need to include explicitly 5 sites for each lead on each side, because we apply outgoing or incoming boundary conditions chosen so as to give the same result as explicit inclusion of semi-infinite leads into our calculation.

The total Hamiltonian for the sample and leads reads:

$$\mathcal{H} = \sum_{n=1}^{N_c} \sum_{i=-\infty}^{\infty} \left[ \left( t_{i,n} c_{i,n}^\dagger c_{i+1,n} + h.c. \right) + \epsilon_{i,n} c_{i,n}^\dagger c_{i,n} \right]$$

$$+ \sum_{i,i'=1}^p \sum_{n,n'=1}^{N_c} v_{i,n;i',n'} c_{i,n}^\dagger c_{i',n'} \quad (10)$$

where  $t_{i,n} = -t$  and  $\epsilon_{i,n} = \epsilon_0$  for all  $i \leq 0$  or  $i \geq p$  (i.e., along the semi-infinite leads) whereas inside the sample these parameters are given by Equations (6) and (7).

### B. Formula for longitudinal conductance

We calculate the longitudinal conductance using the formalism derived in Ref. [28], where it is shown that as a function of Fermi energy  $E_F$ :

$$\sigma_{xx}(E_F) = \frac{e^2}{h} \sum_{ab} v_a v_b |G_{ba}^{R,A}(z, z', E_F/\hbar)|^2 \quad (11a)$$

$$= \frac{e^2}{h} \text{Tr}(t^\dagger t), \quad (11b)$$

Here,  $z$  ( $z'$ ) are positions in the asymptotic regions of the left (right) leads, which are perfect conductors.<sup>29</sup> Also,  $v_{a(b)}$  are group velocities in channels  $a$  ( $b$ ) of the corresponding left (right) lead. The Green's function  $G_{ba}^{R,A}(z, z', E_F/\hbar)$  for a continuous system is:<sup>28</sup>

$$G_{ba}^{R,A}\left(z, z', \frac{E_F}{\hbar}\right) = \int \int d\mathbf{r}_\perp d\mathbf{r}'_\perp u_a^*(\mathbf{r}'_\perp) u_b(\mathbf{r}_\perp) G^{R,A}\left(\mathbf{r}, \mathbf{r}', \frac{E_F}{\hbar}\right) \quad (12)$$

The above equation is simply a projection of the full Green's function  $G^{R,A}(\mathbf{r}, \mathbf{r}', E_F/\hbar)$  onto the transverse modes  $u_{a,b}$  of the leads. In the asymptotic regions of the leads, the conductance becomes independent of  $z$  and  $z'$  in Eq. (11a) because there is no dissipation in the leads.<sup>28</sup> In our model each lead is composed of independent 1D chains, each representing a transverse mode (or channel). As a result, the subscripts  $a$  and  $b$  in Eq. (11a) should be replaced by indexes of different 1D chains on the left and right sides, respectively. Eq. (11b) is the Landauer formula for perfect-conductor leads,<sup>24,29</sup> which we now identify with Eq. (11a) by analyzing the structure of the Green's function.

In Ref. [28], Eq. (11a) is derived for a continuous model; the derivation can be replicated with minor modifications for a discretized system such as ours. The Green's function is now labeled  $G^R(i, n; j, m; E/\hbar)$ , where  $i$  and  $j$  replace the locations  $z, z'$  of the continuous model, whereas  $n, m$  replace the channel indexes  $a, b$ . Consider now the scattering state  $|\phi_{n,E}^+\rangle$  of an electron with momentum  $k > 0$  and total energy  $E(k) = \epsilon_0 - 2t \cos(ka)$  injected along the  $n^{\text{th}}$  channel of the left lead. The scattering state is a solution of the Lippman-Schwinger equation:

$$|\phi_{n,E}^+\rangle = |\phi_{n,k}^s\rangle + \frac{1}{E - \mathcal{H}_0 + i0} (\mathcal{H} - \mathcal{H}_0) |\phi_{n,E}^+\rangle. \quad (13)$$

Here,  $|\phi_{n,k}^s\rangle$  is the incident wave along the left chain, defined by  $\langle j, m | \phi_{n,k}^s \rangle = \delta_{n,m} e^{ikj}$ , which is an eigenstate with energy  $E$  of the Hamiltonian  $\mathcal{H}_0$  defined by

$$\mathcal{H}_0 = \sum_{n=1}^{N_c} \sum_{i=-\infty}^{\infty} \left[ \epsilon_0 c_{i,n}^\dagger c_{i,n} - t \left( c_{i,n}^\dagger c_{i,n+1} + h.c. \right) \right].$$

In other words,  $\mathcal{H}_0$  describes  $N_c$  non-interacting, infinite 1D chains which go through the sample. The scattering Hamiltonian  $\mathcal{H} - \mathcal{H}_0$  is then similar to the sample Hamiltonian  $\mathcal{H}_s$  [see Eq. (9)], except that  $\epsilon_{i,n} \rightarrow \epsilon_{i,n} - \epsilon_0$  and  $t_{i,n} \rightarrow t_{i,n} + t$  in order to account for the terms included in  $\mathcal{H}_0$ . As a result, the scattering potential  $\mathcal{H} - \mathcal{H}_0$  has non-zero matrix elements only inside the sample.

The separation of the total Hamiltonian in this form is very convenient, because the Green's function  $G_0^R(E) = [E - \mathcal{H}_0 + i0]^{-1}$  and corresponding group velocity  $v_k$  for the tight-binding model are well-known:

$$\langle i, n | G_0^R(E) | j, m \rangle = \delta_{n,m} \frac{\exp(ik|j-i|)}{iv_k}, \quad (14a)$$

$$v_k = \sqrt{4t^2 - (E - \epsilon_0)^2}, \quad (14b)$$

$$E = \epsilon_0 - 2t \cos(k). \quad (14c)$$

The quasimomentum  $k$  along the leads is measured in units of  $1/d$ ,  $d$  being the lattice constant of the 1D chains. (Since we assume that all 1D chains are identical, the group velocity and dispersion are the same for all of them. Generalization to non-identical channels is straightforward, but requires inputs for more parameters).

One can now prove (see Appendix) that if  $i < 0$  and  $j > p$ , then  $G^R(i, n; j, m; \frac{E}{\hbar}) = \phi_{n,E}^+(j, m) e^{-iki} / (iv_k)$ . On any of the right-side channels, we have  $\phi_{n,E}^+(j, m) = t_{nm}(E) e^{ikj}$  for all  $j > p$ , where  $t_{nm}(E)$  is the amplitude of probability of transmission from the left channel  $n$  into the right channel  $m$  of an electron with energy  $E$ . Plugging this asymptotic form of  $G^R$  into Eq. (11a) leads to the Landauer formula, Eq. (11b), i.e.  $\sigma_{xx}(E_F) = e^2/h \sum_{n,m} |t_{nm}(E_F)|^2$ .

The question, then, is how to efficiently calculate the transmission coefficients. In principle, one needs to solve the Lippman-Schwinger equation (13) which, in turn, implies finding the retarded Green's function  $G^R(E)$  from the Dyson equation (see Appendix). The essential difficulty for the numerical calculation is to contain the infinite system in a finite-size scheme of computation with appropriate boundary conditions. Our solution to this problem allows us to find the scattering solution in a very elegant and economic way, which also avoids difficulties related to choosing the "proper" value for the small imaginary parameter in the denominator.

To illustrate our solution, assume first, for simplicity, that there is only one channel in both the left, and the right-side leads. Consider the solution of the following inhomogeneous system of linear equations:

$$\begin{pmatrix} e^{-ik} & -1 & 0 & 0 & \cdots & 0 & 0 & 0 & 0 \\ t & E - \epsilon_0 & t & 0 & \cdots & 0 & 0 & 0 & 0 \\ 0 & t & E - \epsilon_0 & t & \cdots & 0 & 0 & 0 & 0 \\ \cdots & \cdots & \cdots & \cdots & \cdots & \cdots & \cdots & \cdots & \cdots \\ 0 & 0 & 0 & 0 & \cdots & t & E - \epsilon_0 & t & 0 \\ 0 & 0 & 0 & 0 & \cdots & 0 & t & E - \epsilon_0 & t \\ 0 & 0 & 0 & 0 & \cdots & 0 & 0 & -1 & e^{-ik} \end{pmatrix} \begin{pmatrix} \phi(-M+1) \\ \phi(-M+2) \\ \phi(-M+3) \\ \cdots \\ \phi(p+M-2) \\ \phi(p+M-1) \\ \phi(p+M) \end{pmatrix} = \begin{pmatrix} -e^{-ik(M-2)} \\ te^{-ik(M-1)} \\ 0 \\ \cdots \\ 0 \\ 0 \\ 0 \end{pmatrix}, \quad (15)$$

where sites  $-M+1, -M+2, \dots, 0$  are on the left-side lead and sites  $p+1, \dots, p+M$  are on the right-side lead, and  $E = \epsilon_0 - 2t \cos k$ , with  $k > 0$ . The matrix in this equation is simply the matrix  $\langle i|E - \mathcal{H}|j \rangle$ , dressed by the first and last lines and columns. Along the lead sites the matrix has the simple form of a hopping Hamiltonian, whereas inside the sample, i.e. for sites between 1 and  $p$ , it contains the full Hamiltonian of the sample. One can now check, using iterations and starting from site  $-M+1$ , that the general solution on the left-side lead is of the form  $\phi(n) = e^{ikn} + \phi(-M+1)e^{-ik(M-1+n)}$  for all  $-M+1 < n < 0$ . In other words, it consists of an incoming wave with unit amplitude, and an outgoing wave with amplitude  $|\phi(-M+1)|$ . On the other hand, starting from the site  $p+M$ , one finds that the general solution on the right-side lead is of out-going type  $\phi(n) = \phi(M+p)e^{ik(n-M-p)}$  for all  $n > p$ . Since the matrix is non-singular, this inhomogeneous system has a unique solution which fixes the values of  $\phi(-M+1)$  and  $\phi(M+p)$ . As a result, we can identify directly the reflection coefficient for the given energy  $E$  as  $r(E) = \phi(-M+1)$  and the transmission coefficient  $t(E) = \phi(p+M)$ .

This approach has a number of considerable advantages. First of all, the number of sites  $M$  kept on the left and right-side leads is inconsequential, as long as it is greater than 2; the solution obtained through the matching of the wavefunction inside the sample is precisely the same as for semi-infinite leads. In our simulations, we keep 5 sites for each 1D channel ( $M = 5$ ). The equivalence of the solution of this finite system with that of a system with semi-infinite leads also implies that while we work numerically with finite matrices, we have a continuous energy spectrum  $E(k) = \epsilon_0 - 2t \cos k$  for the electrons injected into the leads (generally, finite systems have a discrete spectrum). Thirdly, there is no need to introduce an infinitesimally small parameter  $i0$  as in Eq. (13), since the first and last line of the matrix insures that it is no longer singular. Choosing the right value for the small imaginary part is always difficult in numerical calculations and has to be done very carefully in the case of a transfer matrix.<sup>35</sup> With our approach, we take the limit  $\eta \rightarrow 0$  trivially and obtain the exact numerical solution. Finally, one can use various entries on the right-hand side of the inhomogeneous system. In our calculations, we actually use a more efficient formulation, in which all coefficients on the right-hand side,

except the third entry, are zero, i.e. the equation is  $(E - \mathcal{H})\phi = B$ , where  $B^T = (0, 0, 1, 0, 0, \dots)$ . One can verify that this choice injects on the left lead, to the right of the 3<sup>rd</sup> site, an incoming wave with amplitude  $1/(2it \sin k)$  plus an outgoing wave, meaning that in this case,  $t(E) = 2it \sin k \cdot \phi(M+p)$ . In this case (see Appendix)  $\phi(n) = G^R(-M+1, n, E)$ , i.e. some of the matrix elements of the retarded Green's function are produced. Given the identity of Equations (11a) and (11b), the two formulations are equivalent, but the second is numerically more efficient.

The generalization to the case with  $N_c$  left and  $N_c$  right channels is straightforward. As already stated, we keep only 5 sites for each of the left and right-side 1D channels, implying that  $-4 \leq i \leq p+5$ . As a result the total dimension of the matrix  $A = E - \mathcal{H}$  is  $N_A = pN_c + 5 \times 2 \times N_c$ , where  $N_cp = N$  is the total number of states in the LLL. The matrix elements of  $A$  equal the values of  $\langle i, n|E - \mathcal{H}|j, m \rangle$  for all  $i, n$  and  $j, m$  values, except for  $\langle -4, n|A|-4, n \rangle = \langle p+5, n|A|p+5, n \rangle = \exp(-ik)$  and  $\langle -4, n|A|-3, n \rangle = \langle p+4, n|A|p+5, n \rangle = -1$  for all  $n = 1, \dots, N_c$ . This insures that proper out-going solutions are selected for each channel.

We then solve  $n_0 = 1, \dots, N_c$  systems of inhomogeneous equations of the type  $\sum_{j,m} A_{in,jm} X_{n_0}(j, m) = B_{n_0}(i, n)$ , where  $B_{n_0}(i, n) = \delta(n - n_0)\delta(i + 2)$ , i. e. corresponds to an electron injected into the  $n_0^{\text{th}}$  left-side channel. As discussed, the transmission coefficients are then  $t_{n_0,m} = 2it \sin k X_{n_0}(p+5, m)$  (one could choose any sites between  $p+2$  and  $p+5$ ), leading to the total longitudinal conductance at energy  $E = \epsilon_0 - 2t \cos k$  to be

$$\sigma_{xx}(E) = \frac{e^2}{h} 4t^2 \sin^2 k \sum_{n_0=1}^{N_c} \sum_{m=1}^{N_c} |X_{n_0}(p+5, m)|^2 \quad (16)$$

Despite having a very large dimension, the matrix  $A$  is very sparse, and the  $N_c$  similar sets of linear equations  $AX = B$  for a given energy  $E$  can be solved very efficiently using the SuperLU<sup>36</sup> packages. This approach is much faster than direct diagonalization and is particularly well suited for parallelization; as a result, a dense grid of energy values  $E$  can be investigated. We used a cluster of 25 CPUs to scan different energy values in parallel. A typical run lasts for about 10 hours and generates 5000 data points of  $\sigma_{xx}(E)$ .

### C. A toy model

In this section, we analyze the longitudinal conductance for a simple toy model. This allows us to understand the general effect of the lead parameters  $t$  and  $\epsilon_0$  on longitudinal conductance  $\sigma_{xx}(E)$ . As shown in the following section, the shape of the curves  $\sigma_{xx}(E)$ , especially for small or no disorder, is rather surprising at first sight. It consists of large numbers of very thin resonant peaks superimposed over a broad maximum. These sharp resonance peaks are not numerical errors, and do not signal singularities of the type expected in Green's functions.<sup>17</sup> (In fact, since we deal with an infinite system, one expects a continuous cut, not individual singularities, in the Green's functions.) Zooming in the energy scale shows that these peaks are features whose width scale inversely proportional to the size of the sample (i.e. region between the leads). These resonance peaks have the same origin as the peaks in the differential conductance of molecules attached to metal contacts,<sup>32,33,34</sup> i.e. they correspond to resonant tunneling through the system. However, our 2DES is different from a molecule in that it contains about  $10^4$  internal states, hence in a small energy interval there can be a large number of such resonance peaks.

A simple toy model that helps in clarifying the origin of these resonance peaks is that of an  $n$ -bond tight-binding model with hopping  $t_2$  sandwiched between two semi-infinite tight-binding chains with hopping  $t_1$  (on-site energies are all zero for simplicity). Figure 2 shows an example of the toy model.

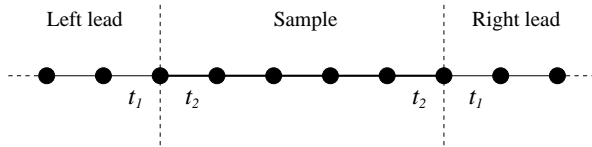


FIG. 2: A sketch of the toy model. The “sample” with  $n = 5$   $t_2$  bonds is connected to semi-infinite leads with  $t_1$  bonds.

We assume  $t_2 < t_1$ ; transmission is then vanishing for  $|E| > 2t_2$ , since the middle section (the “sample”) does not support propagating modes at those energies. The reflection and transmission coefficients on the two interfaces (dashed line in Fig. 2) can be readily computed, and the total transmission rate is calculated either by summing up multiply reflected waves, as for a Fabry-Perrot interferometer, or by solving the Schrödinger's equation directly. The final result is summarized below for a given energy  $E$ :

$$\begin{aligned} E &= -2t_1 \cos(k_1) = -2t_2 \cos(k_2) \\ x &= t_1 \sin(k_1), \quad y = t_2 \sin(k_2), \\ \alpha &= x + y, \quad \beta = x - y \\ T(E) &= \frac{16x^2y^2}{\alpha^4 + \beta^4 - 2\alpha^2\beta^2 \cos(2nk_2)} \end{aligned}$$

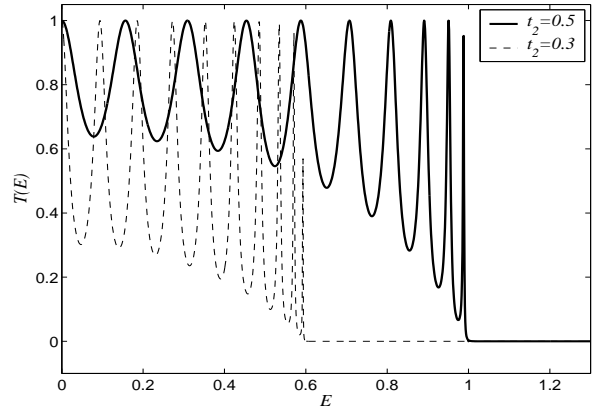


FIG. 3: Transmission rate for the toy model corresponding to  $n = 20$ ,  $t_1 = 1$  and  $t_2 = 0.5$  and  $0.3$  respectively.  $T(E)$  is a symmetric function, so only the interval  $E > 0$  is shown.

We can see from the last equation that  $T(E) = 1$  for all energies for which  $\cos(2nk_2) = 1$ , leading to the appearance of a series of thin peaks at the corresponding energies. The width of each resonance peak is roughly  $1/n$  of the band width, i.e. it is inversely proportional to the system size, as indeed observed in Fig. 3. The minima between neighboring peaks correspond to  $T(E) = 4x^2y^2/(x^2 + y^2)^2$ , and are located at energies for which  $\cos(2nk_2) = -1$ . Thus, the larger the system, the more and sharper such resonance peaks appear. This toy model also provides a check for our numerical scheme, both in the single and the multiple-channel cases.

The decrease in  $T(E)$  from its maximum value of 1 is not due to the resistivity of the “sample” itself, since there is no scattering inside the sample in this toy model. Instead, it results from the resistance of the contacts, which is due to the mismatch  $t_1 \neq t_2$ . (If  $t_1 = t_2 \rightarrow \beta = 0 \rightarrow T(E) = 1$  at all energies). In fact, if the “sample” strip is connected to left and right leads in an infinitely smooth manner, the conductance simply becomes  $e^2/h$  within the overlap of the spectrum of the “sample” with the spectrum of the leads. Similar oscillating behavior in conductance due to contact reflection was previously studied in Ref. [37], where the conductance through a short and narrow ballistic channel is calculated exactly. The oscillatory behavior is attributed to the “*longitudinal resonant electron states, the electronic quantum analog of the acoustic resonant modes of an open organ pipe*”. The toy model we introduced above offers a good analogy to the continuous ballistic channel.

In our calculation, we want to concentrate on the physics inside the sample, therefore we want to minimize the additional resistance from the contacts, which introduces these extra features in the conductance when disorder inside the sample is small. As a result, we have to adjust the value of  $t$  so that it is close to the magnitude of the matrix elements  $t_{i,n}$  of  $H_s$ . On the other hand, the Fermi energy in the calculation is always required to be within the spectrum of the leads,  $E_F \in [\epsilon_0 - 2t, \epsilon_0 + 2t]$ ,



so that the leads behave like perfect conductors. To satisfy this condition without using a large  $t$  value (which leads to impedance mismatch), we set the on-site energy  $\epsilon_0$  at  $E_F$  in each round of calculation, meaning that the leads have a “floating” spectrum. The floating spectrum is certainly not present in any experiments. We use it as a simple way to save computational power. We have verified that such “floating” leads do behave as perfect metals in the simulation, and that small variations of the parameters  $\epsilon_0$  and  $t$  do not change the main features of the numerical results.

The appearance of the large number of resonance peaks also illustrates the evolution from small quantum mechanical systems to large macroscopic systems. Quantum mechanical quantities like  $\sigma(E_F)$  become rapidly oscillating functions as the size of the system is increased. If the energy scale for such oscillations is smaller than the resolution of the measurement or the temperature smearing, the measurable physical quantity is a certain average of this rapidly changing function within the characteristic energy interval. In theory, numerical microscopic calculations become inefficient for large systems, because one has to sample very many energy values to obtain a good picture of the rapidly changing function. In our case, we provide curves more suitable for comparison with the experiment, by convoluting the zero-temperature conductance with a sampling function:

$$\bar{\sigma}_{xx}(\mu, V, T) = \int_{-\infty}^{+\infty} \rho_T(\mu, V, \epsilon) \sigma_{xx}(\epsilon) d\epsilon, \quad (18a)$$

$$\rho_T(\mu, V, \epsilon) = \frac{1}{V} \left[ \frac{1}{e^{\frac{\epsilon - \mu - V/2}{kT}} + 1} - \frac{1}{e^{\frac{\epsilon - \mu + V/2}{kT}} + 1} \right]. \quad (18b)$$

Here,  $\bar{\sigma}$  is the measured conductance at chemical potential  $\mu$ , temperature  $T$  and voltage difference between the two edges of the sample  $V$  (estimated to be of order  $10^{-6}$  eV). This formula is appropriate for non-interacting electrons. One can verify that at zero temperature,

$$\rho_0(\mu, V, \epsilon) = \frac{1}{V} [\Theta(\mu + V/2 - \epsilon) - \Theta(\mu - V/2 - \epsilon)].$$

When  $V \rightarrow 0$ ,  $\rho_T \rightarrow -dn_{EF}(T, \eta)/d\eta$ , where  $n_{EF}(T, \eta) = \left[ \exp\left(\frac{\eta - E_F}{kT}\right) + 1 \right]^{-1}$  is the Fermi-Dirac distribution.

### III. NUMERICAL RESULTS

In this section, we present representative results from our calculations. We analyze the interplay between disorder and periodic potentials of various strengths, starting with the case of no disorder (pure periodic potential).

In Fig. 4, the longitudinal conductance of a small sample with only square periodic potential is shown. There are only 1860 electronic states inside the sample, distributed over 30 channels and the magnetic field is such that  $\phi/\phi_0 = q/p = 2$ . Because there is no disorder, different conduction channels do not couple to each other, and

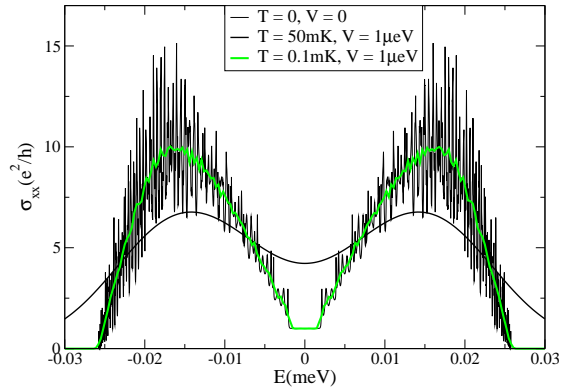


FIG. 4: Longitudinal conductance of a small sample with square periodic potential but no disorder potential.  $\phi/\phi_0 = q/p = 2$ ,  $B = 5.44$ T,  $L_x = 1.248 \mu\text{m}$ ,  $L_y = 1.17 \mu\text{m}$ , corresponding to a total of 1860 states in the lowest Landau level.

each of them is similar to the simple toy model discussed in the last section. The spectrum of each conduction channel (except one) splits into two subbands as expected for the Hofstadter butterfly corresponding to  $q = 2$ . The channel that does not split corresponds to  $n = 15$  in Eq. (6), where the cosine vanishes and  $\epsilon_{i,n} = 0$  everywhere. Each channel contributes to the conductance for energies inside its own spectrum, and thus we see many sharp resonant peaks on top of a fairly broad conductance curve. As already discussed, the sharp peaks are due to contact resistance, not the sample itself. The underlying broad peaks, on the other hand, are a signature of the sample behavior. They are simply a reflection of the density of states inside the Hofstadter butterfly in the clean model. In the vicinity of  $E = 0$ , we see that  $\sigma_{xx}$  is bounded by a series of staircases, each of which marks the edge of the spectrum of a different conduction channel. Thus, the curve for  $T = 0$  (thin black line) is understood as a superposition of many 1D chains similar to the toy model shown in Fig. 3. The two solid curves in Fig. 4 are the “measured”  $\bar{\sigma}_{xx}$  given by Eq. (18), corresponding to  $V = 1 \mu\text{eV}$  and  $T = 0.1$  and  $50$  mK. At large temperatures, the resonance peaks are smeared and only the two broad peaks are visible, whereas for small temperature more detailed features are revealed.

Figure 5 shows  $\sigma_{xx}$  of a sample with only triangular periodic potential at  $q/p = 3$ . From the semi-log inset, we can see gaps between the  $q = 3$  expected adjacent subbands. Since the triangular potential is not particle-hole symmetric (unlike the square potential) the subbands are no longer symmetrically placed with respect to  $E = 0$ . In the smaller gap, the conductance is not vanishing, although it is over 40 orders of magnitude smaller than inside the band. This is a consequence of the fact that the sample is finite and tunneling across it is possible even in the gap region (although with extremely low probability).

Figure 6 shows the calculated longitudinal conductance



of a sample with triangular potential and very small disorder, at  $q/p = 7/3$ . In the absence of disorder, we expect  $q = 7$  subbands to appear asymmetrically in the spectrum. The small disorder closes some of the gaps, and only three main subbands are distinguishable in  $\sigma_{xx}$ . (Each of the three visible subbands is actually a collection of 2 or 3 of the subbands expected in the absence of disorder). The three curves are the same data measured at different temperature and different voltage drops across the sample. As expected, at low temperature and low voltage drop, the measured conductance reveals a variety of resonance peaks on top of each broad conductance feature. From the semi-log plot in the inset, one can see the gap between the left subband and central subband is wide open, whereas the smaller gap between the center and right subbands is partially filled-in by disorder (the value of  $\sigma_{xx}$  inside the gap is of order  $10^{-5}$ , as opposed to  $10^{-40}$  in the absence of disorder, see Fig. 5). This proves that narrow subbands are more easily affected and therefore more likely to be closed by even small disorder, as one would expect on general grounds. For higher temperatures and/or voltage drops, the sharp resonance peaks are averaged out and one obtains relatively smooth curves with broad peaks reflecting the density of states and degree of localization of the sample.

In contrast to the previous cases, Fig. 7 shows the longitudinal conductance for a sample with only disorder potential (thick line) and disorder plus a weak triangular periodic potential (dashed line). In the disorder-only case we see a single broad peak marking the conventional integer quantum Hall transition. The curve measured at  $T = 1mK$  and  $V = 1\mu eV$  is relatively smooth, and its flat top at unit conductance indicates the existence of one semi-classical orbit extending between the two opposite edges. This semi-classical orbit can be seen in Fig. 8, where we display the disorder potential used for this cal-

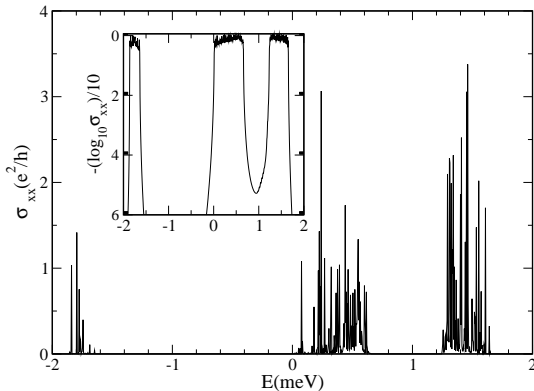


FIG. 5: Longitudinal conductance for pure triangular periodic potential with  $A = 0.01$  meV (no disorder) and  $q/p = 3$  ( $B = 9.42T$ ).  $L_x = 2.004\mu m$ ,  $L_y = 2.028\mu m$ . This sample has 9256 states in the LLL, divided into 52 channels. The inset shows a semi-log plot of the original dataset.

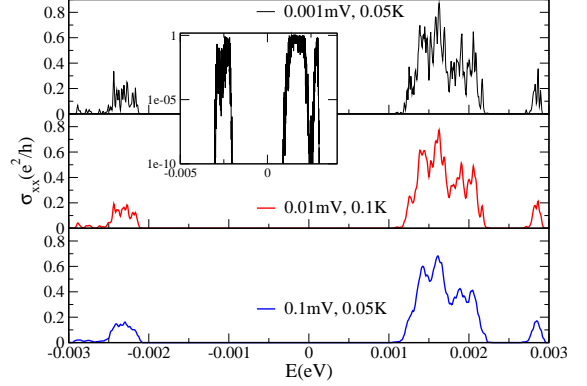


FIG. 6: Longitudinal conductance for triangular periodic potential plus weak disorder, for  $q/p = 7/3$  ( $B = 7.33T$ ).  $L_x = 1.998\mu m$ ,  $L_y = 2.028\mu m$ . This sample has 7176 states divided into 52 channels. The inset shows a semi-log plot of the dataset. The amplitude of disorder is about 1meV, which is only a fraction of the size of the largest gap. However, some of the expected smaller gaps are already filled in by disorder.

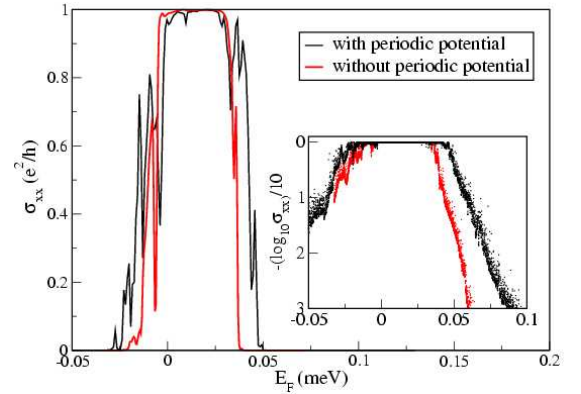


FIG. 7: Longitudinal conductance for a large disorder potential.  $L_x = 2.432\mu m$ ,  $L_y = 2.418\mu m$ ,  $B = 4.71T$ . The thick line corresponds to disorder only, while the thin line corresponds to disorder plus a small periodic potential ( $A = 0.01meV$ ,  $p/q = 2/3$ ). In both cases  $T = 1mK$  and  $V = 1\mu eV$ . The inset is a semi-log plot of the original datasets showing the increase of conductance in the off-resonance tunneling regime, induced by the small periodic potential.

culution. The conduction peak is not centered at  $E = 0$  (center of the LLL level) because the disorder potential is not fully particle-hole symmetric. However, if one symmetrizes the disorder and averages over many disorder realizations, the averaged conductance peak would likely be a smooth Lorentzian-type function. The finite (small) width is due to the finite size of the sample: all wavefunctions with  $x$ -axis localization length larger than  $L_x$  can transport electrons between the leads.

As expected, the addition of a weak periodic potential is not enough to open gaps between the  $q = 3$  subbands

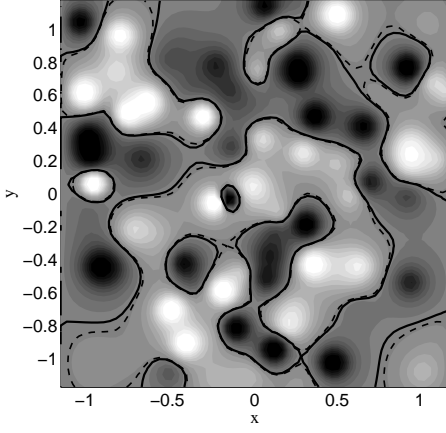


FIG. 8: Contour plot of the disorder potential used to calculate the conductance of Fig. 7. Solid lines are equipotentials for 0 meV, and dashed lines for 0.025 meV. These energies are located within the central peak of conductance. Parts of the contour go along the edge at  $y = \pm L_y/2$ .

of the corresponding Hofstadter butterfly; the amplitude of the periodic potential is only a small fraction of the bandwidth of the disorder-broadened Landau level. However, the small periodic potential still has a sizable effect on the longitudinal conductance: the magnitude of the off-peak conductance has clearly been increased (see the inset) especially on the high energy side. Also, the width of the central peak is increased by an amount comparable to the magnitude of the periodic potential  $A$ , with several more peaks separated by clear valleys appearing on both sides of the central peak.

Figure 9 shows another example of the effect of a weak

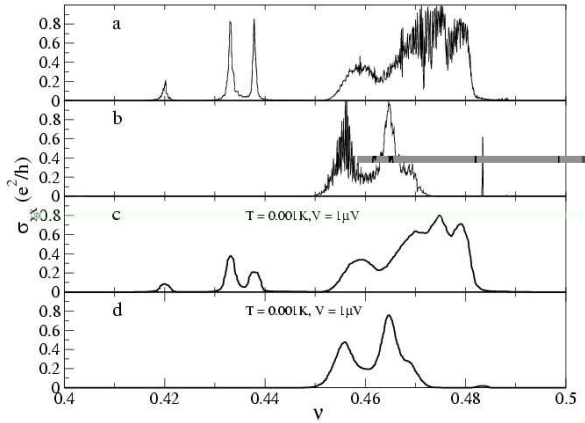


FIG. 9: Another example of a weak triangular potential imposed on a large disorder potential. Here,  $\sigma_{xx}$  is plotted as a function of filling factor  $\nu$ . Panels (a) and (c) show the results with both periodic and disorder potentials, panels (b) and (d) are for disorder only. Panels (a) and (b) are  $T = V = 0$  data, panels (c) and (d) are measured at  $T = 1$  mK and  $V = 1 \mu\text{V}$ . Parameters are:  $B = 7.85$  T,  $p/q = 2/5$ ,  $L_x = 2.432 \mu\text{m}$ ,  $L_y = 2.418 \mu\text{m}$ , 11036 states divided in 62 channels.

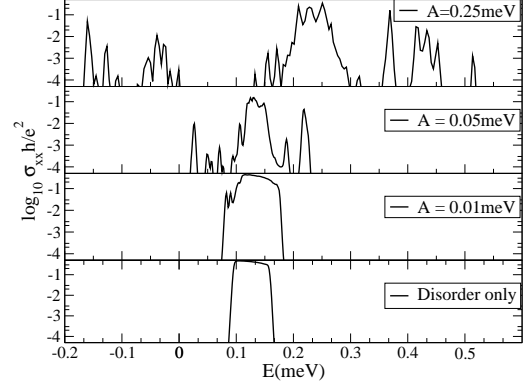


FIG. 10: Longitudinal conductance of a sample with a fixed disorder potential but varying strength of triangular periodic potential. Parameters for this sample are:  $L_x = 3.107 \mu\text{m}$ ,  $L_y = 2.964 \mu\text{m}$ ,  $p/q = 2/5$ ,  $B = 7.85$  T, leading to 16872 states divided amongst 76 channels. The data corresponds to  $T = 1$  mK and  $V = 1 \mu\text{eV}$ .

periodic potential on  $\sigma_{xx}$ . In this case, we plot  $\sigma_{xx}$  against the filling factor  $\nu(E)$  calculated as described in Ref. [17]. For disorder only [panel (b) and (d)], we see a narrow, double-peaked conductance near half-filling, in agreement with the general expectation for the IQHE (the double-peak structure is an artifact of the particular disorder realization used in this simulation). When a small periodic modulation is added [panel (a) and (c)] the conductance shows a much more complex shape: the central peak is broadened considerably, and several extra peaks appear on the low-filling side.

Finally, Fig. 10 shows the conductance of a disordered sample for varying strengths of the periodic potential. The disorder potential, which is kept fixed, is plotted in Fig. 11. For a strong periodic modulation as compared to the disorder ( $A = 0.25$  meV, upper panel), the  $q = 5$  subbands expected in the Hofstadter butterfly at this magnetic field are beginning to emerge. On the other hand, in the disorder-only case (lowest panel) we see a single, smooth conductance peak corresponding to the small energy interval where percolations through the sample is established. Our results show that the interpolation between the two cases shows interesting and non-trivial behavior. Although when  $A = 0.05$  meV the disorder is large enough to completely erase the butterfly structure, the weak periodic modulation has a non-trivial signature reflected by large numbers of peaks on both sides of the disorder-only main conductance peak. The physical origin of these extra peaks has been carefully analyzed in Ref. [17], where we argued that even a weak periodic potential can efficiently create supplementary percolation paths through the sample for energies within a range of the order  $A$  from the critical region. Here, we see the signatures of these states in the longitudinal conductance as well-defined peaks within narrow intervals in en-

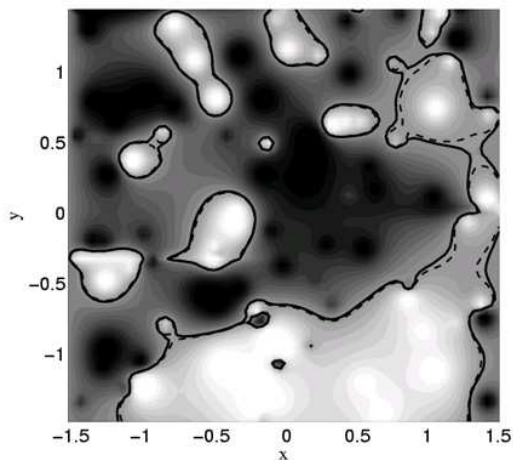


FIG. 11: The disorder potential used in the calculation for Fig. 10, generated by summing random Gaussian scatterers. Solid and dashed contours are at energies 0.11 meV and 0.14 meV respectively, marking the extended orbit responsible for the conductance peak of the pure disorder case.

ergy. Even an extremely small periodic potential (such as  $A = 0.01$  meV) still widens the conductance peak, although there are fewer extra peaks visible in this case.

One technical note: we used a semi-log scale in Fig. 10 because the effect of the periodic potential is not so well revealed in linear scale. This is partially due to the fact that we kept  $t$  for the leads constant for all four cases; this implies that as  $A$  is changed, the impedance mismatch increases and the contact resistance becomes more and more important, suppressing the value of  $\sigma_{xx}$ .

#### IV. CONCLUSION AND DISCUSSIONS

In this paper we use the Kubo-Landauer formalism to compute directly the longitudinal conductance of a 2DES in the presence of periodic modulations as well as disorder. The method employed allows us to study individual disorder realizations and thus to analyze sample-dependent effects. Our method treats the sample as a “big molecule” connected between leads, and is applicable for any type of one-electron potentials, both disordered and periodic. This formulation is particularly suitable for long lengthscale, smooth disorder potentials such as are believed to be dominant in high quality 2DES, because in this case the Hamiltonian is a sparse matrix that can be handled numerically very efficiently. Our simulations are performed for large mesoscopic samples (several microns in linear size), corresponding to roughly  $10^4$  electron states per Landau level. Although this size is still smaller than that of most devices used in IQHE experiments, this type of calculation can help us understand the physical processes in detail. This method can also be very fruitful for investigating transport in various nano-scale devices, and can also be generalized in a

straightforward manner for systems connected to more than two terminals (leads).

Here, we concentrate on the interplay between a short wavelength periodic potential and long wavelength disorder, and their role in determining the longitudinal conductance of the 2DES. The phenomenology in the asymptotic limits has been known for a long time. A pure periodic potential splits the Landau levels into a number of subbands, and the resulting band-structure has fractal properties as a function of the magnetic field. In this case, our simulations show the clearly separated peaks in longitudinal conductance corresponding to each subband. If a weak disorder potential is added, the smaller gaps are closed by disorder, as expected on general grounds. Our results are in good qualitative agreement with previous studies of the weak-disorder case, using SCBA and similar approaches.<sup>13,14</sup> However, unlike our method, the SCBA is valid only for small disorder and gives only disorder-averaged quantities. On the other hand, our method also reproduces the results expected for large disorder (no periodic potential) with long lengthscale, smooth variation. In this case we find a single, relatively smooth peak in the conductance at energies where semiclassical percolated orbits connect the opposite edges, and negligible conductance elsewhere.

The new results come when we investigate the cases where the periodic modulation is comparable, but smaller than the disorder. To our knowledge, this case had not been investigated previously. We find that even a weak modulation has a non-trivial effect on the conductance, with the conduction being significantly enhanced. New sharp peaks in conductance develop around the original conductance peak, increasing its width and creating complex oscillatory features. Although these peaks are clearly due to the periodic modulation, their origin is not simply the Hofstadter structure, which is not relevant for large disorder. The mechanism of enhanced conduction was explained in detail by us in Refs. [16,17]. Basically, the periodic potential helps electrons percolate through flat regions in the disorder landscape and thus connect localized states to form new conductive states. This is in qualitative agreement with recent experimental observations<sup>16</sup> which show distinct patterns of peaks and valleys in the longitudinal conductance of a periodically modulated 2DES, instead of the smooth peak expected for unpatterned samples. However, our calculation is limited to the *band conductance*, which has metallic temperature dependence, and therefore is not suitable to explain the temperature-enhanced conduction in the tail of  $R_{xx}$  seen in the same experiment. We believe that in that region, the conduction is due to hopping among localized states rather than charge transport through extended states. As demonstrated in Ref. [17], a small periodic potential is very effective in increasing the localization lengths and thus the hopping probability.

Our method of computation has a number of limitations. One comes from the fact that it is an exact calculation at zero temperature for a large system. Especially

in the absence of disorder,  $\sigma_{xx}$  is a rapidly oscillating function that requires evaluation at a huge number of energy values in order to get a good sampling for temperature averaging, and this is a major limitation. Secondly, the lead modeling is very elementary, although we can treat the case of semi-infinite leads exactly. The simplicity in describing the leads and their coupling to the sample comes from our ignorance of their detailed physical characteristics. However, one can straightforwardly generalize our method to describe more complicated dispersion relations, and different types of channels and/or couplings to the sample. In particular, the contact resistance due to the mismatch between the leads and the sample should be minimized as much as possible; this can be achieved with a suitable choice of the lead parameters.

The most obvious limitation of this study is that we have little knowledge of the functional form of the disorder and the periodic potential, and how the sample's LL wave functions are coupled to the Fermi sea in the leads. Until such knowledge is available, detailed quantitative comparisons with the experiments are not warranted. We use two simple phenomenological disorder models, and both give qualitatively similar results. Coupled with our understanding of the nature of the wave-function (see Ref. [17]) this gives us the confidence to claim that such effects are genuine and should be observed for smooth, long length scale disorder. If the disorder varies on a much shorter length scale, as may be the case for quantum wires and dots (e.g., in Ref. [20,22]), we believe that a weak periodic modulation will have a very small, if any effect, simply because in this case there are no relatively flat regions in the disorder landscape where the periodic potential plays a dominant role. This is indeed confirmed by simulations we performed for models with short length scale disorder (not shown here), where addition of a weak periodic modulations has no noticeable effect on the longitudinal conductance.

As for the periodic potential, we have been using only the components with shortest reciprocal lattice vectors. However, as experimentalists are designing new devices with enhanced periodic potentials, the higher order Fourier components, as well as inter-Landau band mixing which has not been considered here, might play a role. Such cases can be treated with this formalism, the complications being only of numerical nature. As more accurate models for the sample disorder and modulation, as well as the leads and their coupling, on one hand, and more powerful computational facilities, on the other hand, become available, this formalism will allow for meaningful comparisons with experimental results for transport in mesoscopic systems.

### Acknowledgements

We thank Sorin Melinte, Mansour Shayegan, Paul M. Chaikin and Mingshaw W. Wu for valuable discussions.

This research was supported by NSF grant DMR-0213706 (C.Z.) and NSERC of Canada (M.B.).

### APPENDIX: SCATTERING STATES

In the following we demonstrate the relationship between  $G^R(-2, n_0; j, m; \frac{E}{\hbar})$  and  $\phi_{n_0, E}^+(j, m)$ . The scattering state  $\phi_{n_0, E}^+(j, m) = \langle j, m | \phi_{n_0, E}^+ \rangle$  satisfies the Lippman-Schwinger equation Eq. (13) for  $n = n_0$ , while the retarded Green's function  $G^R(-2, n_0, j, m, \frac{E}{\hbar})$  satisfies a similar Dyson equation:

$$G^R = G_0^R + \frac{1}{E - \mathcal{H}_0 + i0} (\mathcal{H} - \mathcal{H}_0) G^R \quad (\text{A.1})$$

where, for simplicity, we do not write the arguments of  $G^R$  and  $G_0^R$  explicitly. Here  $(E - \mathcal{H}_0 + i0)^{-1} = G_0^R(E)$  is just the formal expression in matrix form, and  $i0$  is an infinitesimally small imaginary number which selects out-going waves in the analytic calculation. The inhomogeneous term in the Dyson's equation has the form given by Eq. (14):

$$G_0^R(-2, n_0, j, m, \frac{E}{\hbar}) = \delta_{n_0, m} \frac{\exp(ik[j+2])}{iv_k} \quad (\text{A.2})$$

We multiply Eq. (13) by  $\frac{e^{2ik}}{iv_k}$  and subtract it from Dyson's equation Eq. (A.2), to obtain:

$$\begin{aligned} \psi = \delta_{n_0, m} \theta(-2-j) \frac{\exp[-ik(2+j)] - \exp[ik(2+j)]}{iv_k} \\ + \frac{1}{E - \mathcal{H}_0 + i0} (\mathcal{H} - \mathcal{H}_0) \psi \end{aligned} \quad (\text{A.3})$$

where  $\psi = G^R(-2, n_0, j, m, \frac{E}{\hbar}) - \frac{e^{2ik} \phi_{n_0, E}^+(j, m)}{iv_k}$ . This equation can be solved by noticing that  $\mathcal{H} - \mathcal{H}_0$  has the same structure as  $\mathcal{H}_s$ , whereas the inhomogeneous term has support only on the  $n_0^{\text{th}}$  lead, outside the sample. It follows that the first order solution  $\psi = -\delta_{n_0, m} \theta(-2-j) \frac{2 \sin[k(2+j)]}{v_k}$  is actually the exact solution, and therefore:

$$\begin{aligned} G^R(-2, n_0, j, m, \frac{E}{\hbar}) = \frac{e^{2ik} \phi_{n_0, E}^+(j, m)}{iv_k} \\ - \delta_{n_0, m} \theta(-2-j) \frac{2 \sin[k(2+j)]}{v_k} \end{aligned} \quad (\text{A.4})$$

This shows that up to a multiplicative constant, the Green's function reproduces the scattering state on the right-side leads ( $j > p$ ), and its asymptotic form there is therefore  $\frac{e^{2ik}}{iv_k} t_{n_0, m} e^{ikj}$ .

- 
- <sup>1</sup> D. R. Hofstadter, Phys. Rev. B **14**, 2239 (1976).
  - <sup>2</sup> G. H. Wannier, Rev. Mod. Phys. **34**, 645 (1962).
  - <sup>3</sup> Dieter Langbein, Phys. Rev. **180**, 633 (1969).
  - <sup>4</sup> P. G. Harper, Proc. Phys. Soc. Lond. A **68**, 874 (1955).
  - <sup>5</sup> M. Ya. Azbel', Zh. Eksp. Teor. Fiz. **46**, 939 (1964); [Sov. Phys.-JETP **19**, 634 (1964)].
  - <sup>6</sup> P. Středa, J. Phys. C: Solid State Phys. **15**, L717 (1982).
  - <sup>7</sup> P. Středa, J. Phys. C: Solid State Phys. **15**, L1299 (1982).
  - <sup>8</sup> A. H. MacDonald and P. Středa, Phys. Rev. B **29**, 1616 (1984).
  - <sup>9</sup> A. H. MacDonald, Phys. Rev. B **29**, 6563 (1984).
  - <sup>10</sup> K. von Klitzing, G. Dorda and M. Pepper, Phys. Rev. Lett. **45**, 494 (1980).
  - <sup>11</sup> Rolf R. Gerhardts, Dieter Weiss, and Ulrich Wulf, Phys. Rev. B **43**, 5192 (1991).
  - <sup>12</sup> D. Weiss, M. L. Roukes, A. Menschig, P. Grambow, K. von Klitzing and G. Weimann, Phys. Rev. Lett. **66**, 2790 (1991).
  - <sup>13</sup> Daniela Pfannkuche and Rolf R. Gerhardts, Phys. Rev. B **46**, 12606 (1992).
  - <sup>14</sup> Ulrich Wulf and A. H. MacDonald, Phys. Rev. B **47**, 6566 (1993).
  - <sup>15</sup> see, for instance, the non-trivial Chern numbers for the square lattice.
  - <sup>16</sup> S. Melinte, M. Berciu, C. Zhou, E. Tutuc, S. J. Papadakis, C. Harrison, E. P. De Poortere, M. Wu, P. M. Chaikin, M. Shayegan, R. N. Bhatt, and R. A. Register, Phys. Rev. Lett. **92**, 036802 (2004).
  - <sup>17</sup> Chenggang Zhou, Mona Berciu and R. N. Bhatt, cond-mat/0401007.
  - <sup>18</sup> S. Melinte, E. Grivei, V. Bayot, and M. Shayegan, Phys. Rev. Lett. **82**, 2764 (1999), and references therein.
  - <sup>19</sup> F. H. Claro and G. H. Wannier, Phys. Rev. B **19**, 6068 (1979).
  - <sup>20</sup> J. A. Nixon and J. H. Davies, Phys. Rev. B **41**, 7929 (1990).
  - <sup>21</sup> John A. Nixon, John H. Davies and Harold U. Baranger, Phys. Rev. B **43**, 12638 (1991).
  - <sup>22</sup> M. Stopa, Y. Aoyagi, Physica B **227**, 61 (1996); M. Stopa, Phys. Rev. B **54**, 13767 (1996); M. Stopa, Phys. Rev. B **53**, 9595 (1996).
  - <sup>23</sup> D. J. Thouless, Phys. Rep. **13C**, 93 (1974).
  - <sup>24</sup> R. Landauer, Philos. Mag. **21**, 863 (1970).
  - <sup>25</sup> P. W. Anderson, D. J. Thouless, E. Abrahams, and D. S. Fisher, Phys. Rev. B **22**, 3519 (1980).
  - <sup>26</sup> Various equivalent forms of Kubo formula for conductivity exist, see for example, R. Kubo, J. Phys. Soc. Jpn. **12**, 570 (1957) or R. Kubo, M. Toda and N. Hashitsume, "Nonequilibrium Statistical Mechanics" (Springer, 1985), also Refs. [6,7]. Ref. [27] offers detailed derivation of different forms, and Ref. [28] proves that in a certain type of model (similar to ours), the Kubo and the Landauer formalisms are equivalent.
  - <sup>27</sup> H. U. Baranger and A. D. Stone, Phys. Rev. B **40**, 8169 (1989).
  - <sup>28</sup> The Kubo formula and the Landauer formula have been found to be equivalent in the current context for longitudinal conductance, see Daniel S. Fisher and Patrick A. Lee, Phys. Rev. B **23**, 6851 (1981).
  - <sup>29</sup> E. N. Economou and C. M. Soukoulis, Phys. Rev. Lett. **46**, 618 (1981).
  - <sup>30</sup> As we introduce the computational method, it will also become clear that in the Landauer formula, the conductance is not strongly dependent on the detailed dispersion relation of the leads.
  - <sup>31</sup> The maximum conductance of the sample with only periodic potential is  $N_c \frac{e^2}{h}$ , i. e. each conduction channel may contribute a maximum of one unit conductance, since in this case there is no coupling between (and therefore scattering into) other channels. Each injected electron either comes out on the other side of the sample (if electron density and magnetic field  $B$  are such that the Fermi level is inside a subband) or is completely reflected back (if Fermi level is in one of the gaps of the Hofstadter butterfly).
  - <sup>32</sup> Magnus Paulsson and Sven Stafström, Phys. Rev. B **64**, 035416 (2001); *ibid* J. Phys.: Cond. Matt. **12**, 9433 (2000).
  - <sup>33</sup> Eldon G. Emberly and George Kirczenow, Phys. Rev. B **64**, 235412 (2001).
  - <sup>34</sup> Alexander Onipko, Yuri Klymenko, Lyuba Malysheva, Phys. Rev. B **62**, 10480 (2000).
  - <sup>35</sup> D. J. Thouless and S. Kirkpatrick, J. Phys. C: Solid State Phys., **14**, 235 (1981).
  - <sup>36</sup> M. Baertschy, T. N. Rescigno, W. A. Issacs, X. S. Li, and C. W. McCurdy, Phys. Rev. A **63**, 022712 (2001). For details of the software used see <http://www.nersc.gov/~xiaoye/SuperLU>
  - <sup>37</sup> G. Kirczenow, Phys. Rev. B **39**, 10452 (1989).